# Comparison of Hypersonic Experiments and PNS Predictions Part II: Aerodynamics

Bilal A. Bhutta* and Clark H. Lewis†
*VRA, Inc., Blacksburg, Virginia 24063*

**Predictions and comparisons with wind-tunnel data are presented for a new three-dimensional parabolized Navier-Stokes (PNS) scheme for predicting perfect-gas and equilibrium-air hypersonic flows around complex three-dimensional configurations. In addition to a predictor-corrector solution and a crossflow-coupled implicit shock fitting, this three-dimensional PNS scheme also involves a new fast and efficient elliptic grid-generation scheme for accurately modeling three-dimensional configurations. The test cases considered cover a Mach number range of 10–20 and an angle-of-attack range of 0–14 deg. The resulting predictions of wall-pressure distributions and force and moment data are compared with available wind-tunnel data and are found to be in excellent agreement under laminar and fully turbulent conditions. Results also show that the new elliptic grid-generation scheme requires only 10–15% more computing time then the simple cylindrical grid-generation scheme; however, it is capable of treating a much wider range of simple-to-complex three-dimensional configurations.**

## Nomenclature

| | |
|---|---|
| *ALPHA* | = angle of attack $\alpha$, deg |
| *CA* | = axial-force coefficient |
| *CN* | = normal-force coefficient |
| *CM* | = pitching-moment coefficient (with respect to the nose) |
| DXMAX | = maximum axial step size |
| *K* | = grid index in the $\xi_3$ direction |
| *L* | = reference length for force and moment coefficients, also grid index in the $\xi_2$ direction |
| *P* | = static pressure |
| *PHI* | = circumferential angle $\phi$, deg |
| *PINF* | = freestream static pressure |
| *PW* | = wall pressure |
| *RN,Rn* | = nose radius |
| *X,x* | = coordinate along body axis |
| *XCP* | = axial location of the center of pressure |
| $\alpha$ | = angle of attack, deg |
| $\xi_2$ | = coordinate measured from the body to the outer bow shock |
| $\xi_3$ | = coordinate measured from the windward to the leeward pitch plane |
| $\phi$ | = circumferential angle measured from the windward side, deg |

## Introduction

ONE of the main objectives of this paper is to present detailed comparisons of the predictions of a new three-dimensional parabolized Navier-Stokes (PNS) scheme with available wind-tunnel data on complex three-dimensional configurations. A brief discussion of the numerical solution scheme used is given in Part I of this paper, which also includes detailed comparisons with available flight and wind-tunnel data on surface heat-transfer distributions for relatively simple blunt conical configurations with/without bent noses. Part II of this paper focuses on complex three-dimensional configurations and provides comparisons of wall-pressure and force and moment data. The elliptical and cylindrical grid-generation schemes used to model these three-dimensional configurations are also described in Part I of this paper. In general, the results show that the predictions of the present three-dimensional PNS scheme are in excellent agreement with available data.

Presented as Paper 90-3068 at the AIAA 8th Applied Aerodynamics Conference, Portland, OR, Aug. 20-22, 1990; received Nov. 15, 1990; revision received Feb. 11, 1991; accepted for publication Feb. 12, 1991. 

*Chief Scientist. Senior Member AIAA.
†President. Associate Fellow AIAA.

## Results and Discussion

The following sections provide comparisons of the present numerical predictions with the corresponding wall-pressure distributions and force and moment data obtained in the Arnold Engineering Development Center's (AEDC) VKF Tunnel C on a 14/7-deg bicone with and without a flat windward surface.[1] In addition, the flow over a 5-deg sphere cone with asymmetric spin tabs is also computed to demonstrate the grid-generation and computational capabilities of the present three-dimensional PNS scheme. The freestream conditions for these cases are summarized in Table 1.

In general, these PNS calculations cover a Mach number range of 10–20 and an angle-of-attack range 0–14 deg (see Table 1). The computational grids used for all these PNS calculations use a near-wall grid spacing of $1.0 \times 10^{-3}$% of the local shock standoff distance. Numerical experience has shown such a fine grid spacing to be adequate for resolving the near-wall temperature and velocity gradients. Typically, the afterbody PNS solutions are started at the sphere-cone tangent point with a small axial step size, which is gradually increased to DXMAX in the afterbody region. As described in Part I of this paper, appropriate VSL blunt-body solution schemes were used to generate the starting solutions for these PNS calculations.

### 14/7-Deg Bicone Calculations With/Without a Windward Flat

This 14/7-deg configuration with/without a windward flat in the aftcone region is shown in Fig. 1. These configurations were tested in the VKF Tunnel C at AEDC by Hahn.[1] The particular tests involved additional configurations and two different total pressure conditions. The freestream conditions chosen for comparison are summarized in Table 1. The freestream Mach number for these conditions was 10, and an angle-of-attack range of 0–14 deg was considered. The flow conditions were assumed to be laminar, and a perfect-gas model was used with a wall temperature of 5400°R. The biconic model used (Fig. 1) had a nose radius (*Rn*) of 0.5 in. and an overall length of 56.566*Rn*. The measured model forces

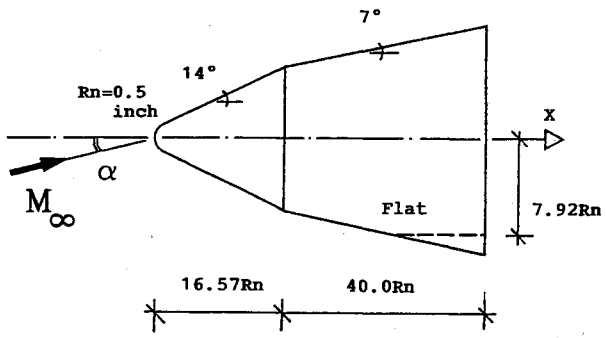


**Fig. 1 The 14/7-deg biconic configuration with and without the windward flat.**

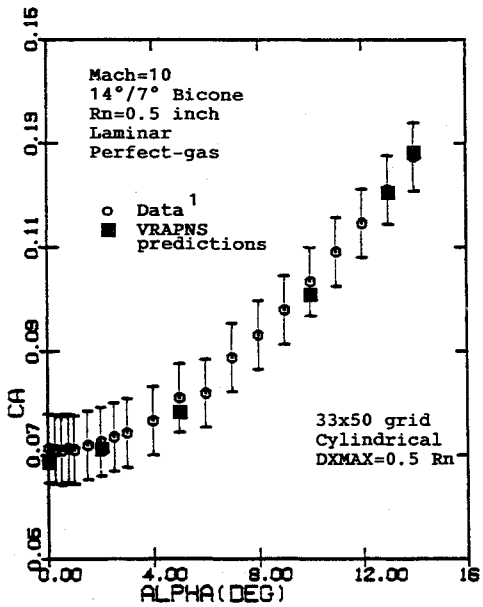


**Fig. 2 Comparison of data and predicted axial-force coefficient for the case 8 calculations.**

and moments were corrected for measured base-pressure effects, and the resulting data were used to obtain the forebody axial-force coefficient (*CA*), normal-force coefficient (*CN*), and pitching-moment coefficient (*CM*). According to Hahn,[1] the uncertainty in the aerodynamic coefficients as determined from the accuracy of the six-component balance and the accuracy of the base pressure transducers for these high-pressure conditions was ±0.0066 in *CA*, ±0.019 in *CN*, and ±0.023 in *CM*. Numerical calculations were done for 0-, 2-, 5-, 10-, 13-, and 14-deg angles of attack, and the predicted forebody force and moment data (with zero base drag) were compared with the corresponding experimental data.

*Straight Bicone Calculations (Case 8)*

The flow over the 14/7-deg bicone geometry (Fig. 1) was predicted at 0-, 2-, 5-, 10-, 13-, and 14-deg angle-of-attack conditions. The force and moment data predicted for these angle-of-attack conditions and the grid sizes used are summarized in Table 2 along with the corresponding computing times on a Cray Y/MP. Briefly speaking, the zero angle-of-attack flow was analyzed using a 150-point and a 50-point grid, and it was observed that the predictions of the two grids were almost identical. Thus, it was concluded that computational grids using 50 point in the axis-normal direction were adequate for these force and moment calculations. The flow at 2-deg angle of attack was studied using two cylindrical grids consisting of uniformly spaced 9 and 33 crossflow planes, respectively. The results indicated that the 9-plane and 33-plane results differed by approximately 10%. Thus, it was decided to use a 33×50 (50 axis-normal points and 33 crossflow planes) grid for all angle-of-attack calculations. For all these calculations the maximum axial step size used (DXMAX) was 0.5*Rn*.

**Table 1 Freestream conditions**

| Quantity | Cases 8-9 | Cases 10 |
|---|---|---|
| W-T/flight[a] | W-T | Flight |
| Mach number | 10.00 | 20.00 |
| Altitude, thousands of ft | — | 100.0 |
| Pressure, psf | 2.588 | 23.14 |
| Temperature, °R | 94.90 | 410.9 |
| Angle-of-attack range, deg | 0.0–14.0 | 0.0 |
| Wall temperature | 540.0 | 2000.0 |
| Gas model | PG[b] | PG |
| Flow type | LAM[c] | TRB[d] |
| Nose radius, in. | 0.50 | 1.00 |

[a]W-T = wind-tunnel conditions, flight = flight conditions.
[b]PG = Perfect-gas model.
[c]LAM = Laminar flow conditions.
[d]TRB = Fully-turbulent flow conditions.

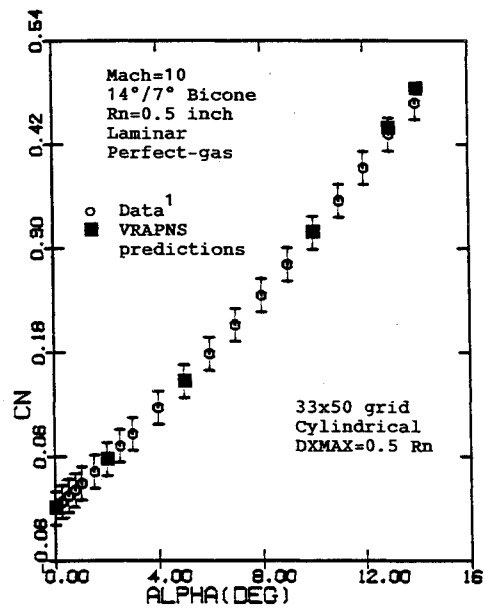


**Fig. 3 Comparison of data and predicted normal-force coefficient for the case 8 calculations.**

The force and moment data of Table 2 are also shown in Figs. 2–5. Figure 2 shows the variation of the axial-force coefficient (*CA*) with angle of attack. These results show that the predictions and data are in close agreement over the entire angle-of-attack range. There seem to be somewhat larger differences at smaller angles of attack than at larger angles of attack; however, these differences are well within the uncertainty bounds of the data. The normal-force and pitching-moment coefficients (*CN* and *CM*) are shown in Figs. 3 and 4, respectively. In this case there is almost perfect agreement at lower angles of attack, whereas slightly larger differences between the predictions and data are seen at larger angles of attack. However, even these differences are well within the uncertainty limits. The variation of the center of pressure (*XCP/L*) is shown in Fig. 5 and also shows excellent agreement between the predictions and the data.

The computing times for these calculations are shown in Table 2 and show that, on the average, these calculations took about 3 min on the Cray Y/MP. The 14-deg angle-of-attack calculation took about 50% longer to do than the corresponding 2-deg case. This is because the numerical complexity, and

**Table 2 Predicted force and moment data and computing times for cases 8 and 9 (Mach 10, perfect-gas, laminar, DXMAX = 0.5*Rn*)**

| Case | AOA,[a] deg | Grid[b] N3×N2×N1 | *CA*[c] | *CN*[c] | −*CM*[c] | *XCP/L*[c] | Time, s[d] |
|---|---|---|---|---|---|---|---|
| 8a | 0 | 1×150×122-C | 0.06868 | — | — | — | 60 |
| 8b | 0 | 1× 50×122-C | 0.06869 | — | — | — | 10 |
| 8c | 2 | 9× 50×122-C | 0.06918 | 0.05197 | 0.02970 | 0.5714 | 35 |
| 8d | 2 | 33× 50×122-C | 0.07098 | 0.05630 | 0.03233 | 0.5743 | 142 |
| 8e | 5 | 33× 50×122-C | 0.07817 | 0.1452 | 0.08378 | 0.5772 | 145 |
| 8f | 10 | 33× 50×122-C | 0.1007 | 0.3186 | 0.1882 | 0.5906 | 161 |
| 8g | 13 | 33× 50×122-C | 0.1210 | 0.4405 | 0.2629 | 0.5969 | 217 |
| 8h | 14 | 33× 50×122-C | 0.1283 | 0.4858 | 0.2909 | 0.5988 | 208 |
| 9a | 0 | 33× 50×122-E | 0.06716 | −0.00957 | −0.00886 | 0.9269 | 143 |
| 9b | 2 | 33× 50×122-E | 0.06826 | 0.04298 | 0.01992 | 0.4636 | 149 |
| 9c | 5 | 33× 50×122-E | 0.07401 | 0.1245 | 0.06463 | 0.5190 | 150 |
| 9d | 10 | 33× 50×122-E | 0.09219 | 0.2826 | 0.1546 | 0.5471 | 161 |
| 9e | 10 | 33× 50×122-C | 0.09213 | 0.2823 | 0.1544 | 0.5469 | 156 |
| 9f | 13 | 33× 50×122-E | 0.1084 | 0.3942 | 0.2195 | 0.5570 | 214 |

[a] AOA = angle of attack.
[b] N1, N2, and N3 are the number of grid points in the streamwise, axis-normal, and crossflow directions, respectively. The notations of C and E mean cylindrical and elliptic grids, respectively.
[c] Reference length = 28.283 in., reference area = 75.784 in.$^2$.
[d] Computing times on Cray Y/MP with CFT77 compiler and autovectorization.

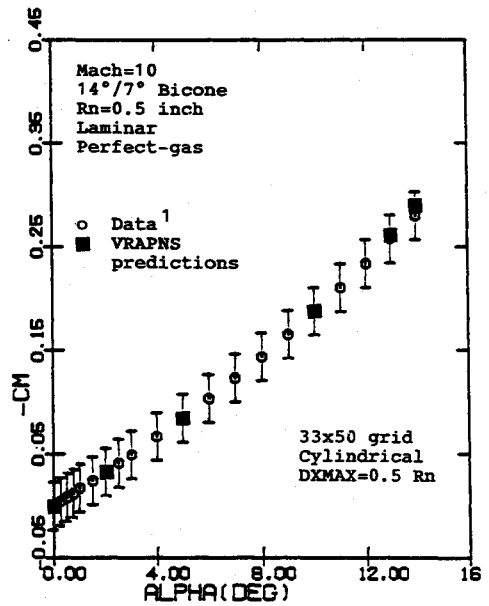


**Fig. 4 Comparison of data and predicted pitching moment coefficient for the case 8 calculations.**

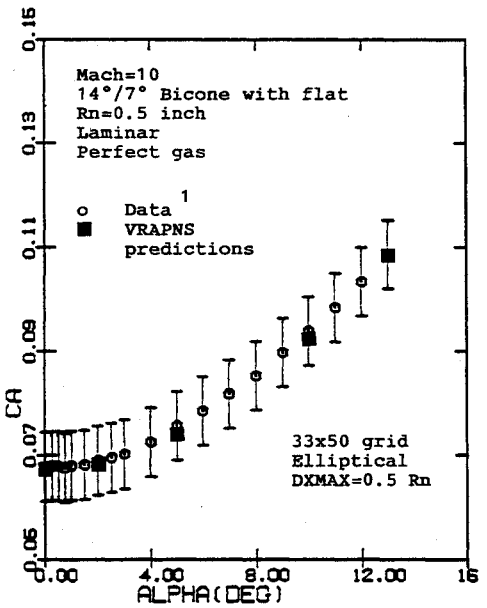


**Fig. 6 Comparison of data and predicted axial-force coefficient for the case 9 calculations.**

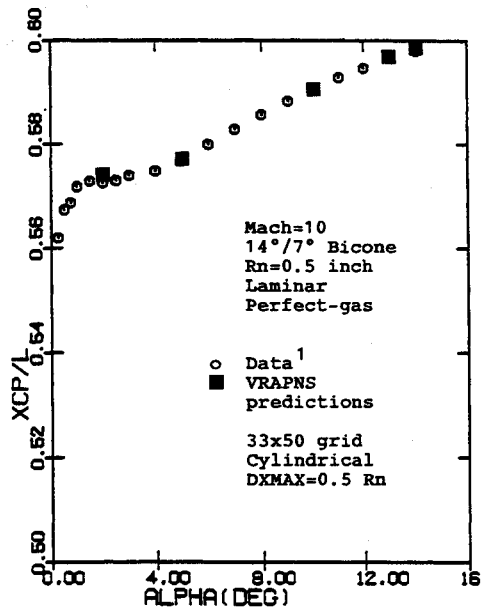


**Fig. 5 Comparison of data and predicted center-of-pressure location for the case 8 calculations.**

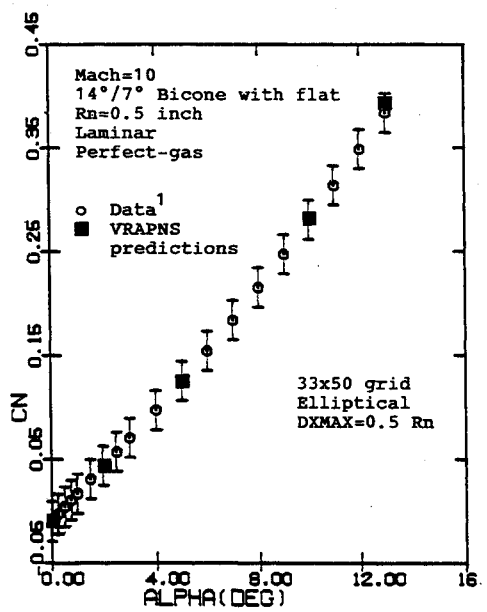


**Fig. 7 Comparison of data and predicted normal-force coefficient for the case 9 calculations.**

thus the required number of solution iterations per step increases with the angle of attack.

*Calculations for Bicone with Windward Flat (Case 9)*

The flow over the 14/7-deg bicone geometry with a windward flat in the aftcone region (Fig. 1) was predicted at 0-, 2-, 5-, 10-, and 13-deg angle of attack conditions. Based on the results of the corresponding straight bicone case (Table 2), it was decided to use a $33 \times 50$ (33 crossflow planes and 50 axis-normal points) elliptic grid with a maximum axial step size of $0.5Rn$. The elliptic grid was used to provide a better numerical modeling of the flat lower surface. The 10-deg angle-of-attack case was also computed using a cylindrical grid for comparison purposes.

The force and moment data predicted for these angle-of-attack conditions and the grid sizes used are summarized in Table 2 along with the corresponding computing times on a Cray Y/MP. Figure 6 shows the variation of the axial-force coefficient ($CA$) with angle of attack. These results show that the predictions and the data are in close agreement over the entire angle-of-attack range. There seem to be slightly larger differences in the 5- to 10-deg angle-of-attack range; however, these differences are small compared to the uncertainty bounds of the data. The normal-force and pitching moment coefficients ($CN$ and $CM$) are shown in Figs. 7 and 8, respectively. In this case there is almost perfect agreement up to 10-deg angles of attack, with slightly larger difference between the predictions and data at 13-deg angle of attack. However, these differences are also small compared to the data uncertainty. The variation of the center of pressure ($XCP/L$) is shown in Fig. 9, and this also shows excellent agreement between the predictions and the data. In short, the predicted force and moment data are in very close agreement with the experimental data over the entire angle-of-attack range considered.

The computing times for these calculations are also shown in Table 2 and show that these calculations took almost the same time as the corresponding straight bicone case. As expected,

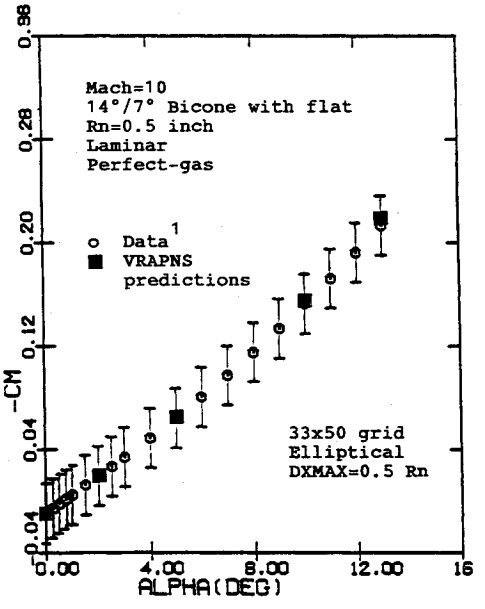


**Fig. 8 Comparison of data and predicted pitching-moment coefficient for the case 9 calculations.**

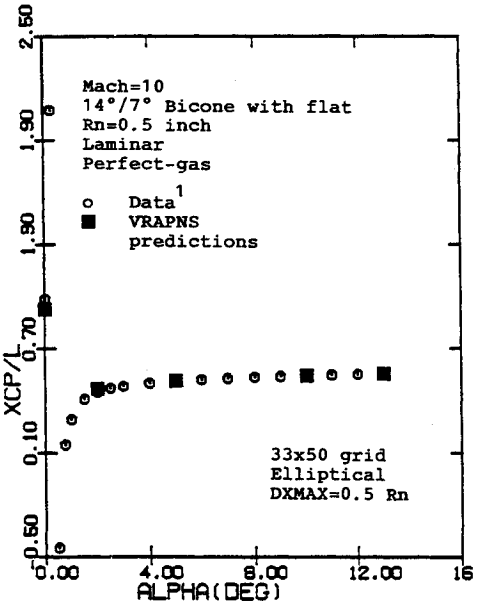


**Fig. 9 Comparison of data and predicted center-of-pressure location for the case 9 calculations.**

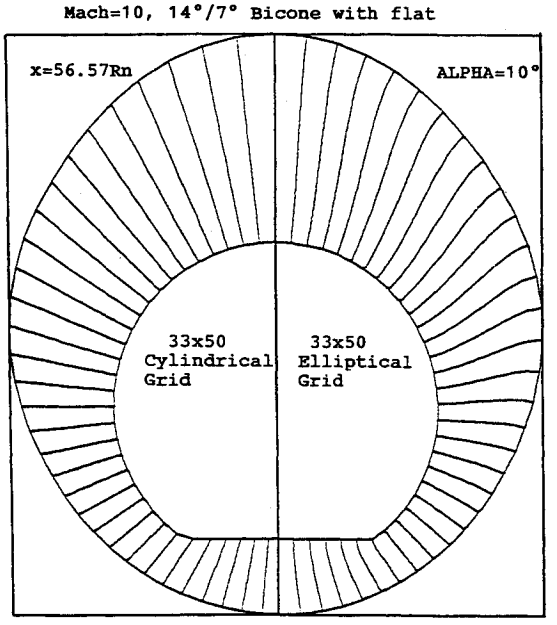


**Fig. 10 Comparison of the $\xi_3 = \text{const}$ coordinate lines at $x = 56.57Rn$ for the bicone with flat at $\alpha = 10$ deg.**

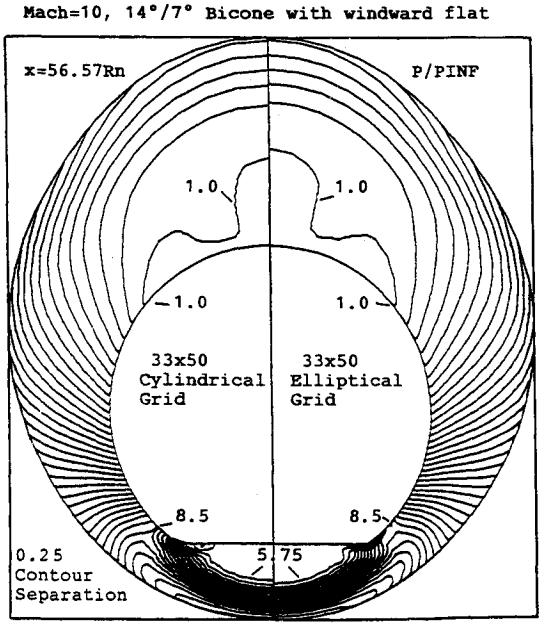


**Fig. 11 Crossflow pressure contours at $x = 56.57Rn$ for the bicone with flat at $\alpha = 10$ deg.**

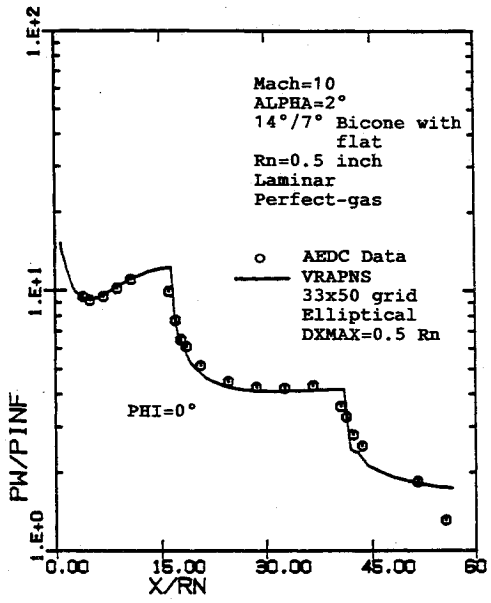


Fig. 12 Axial distribution of windward wall pressure for the bicone with flat at $\alpha = 2$ deg.

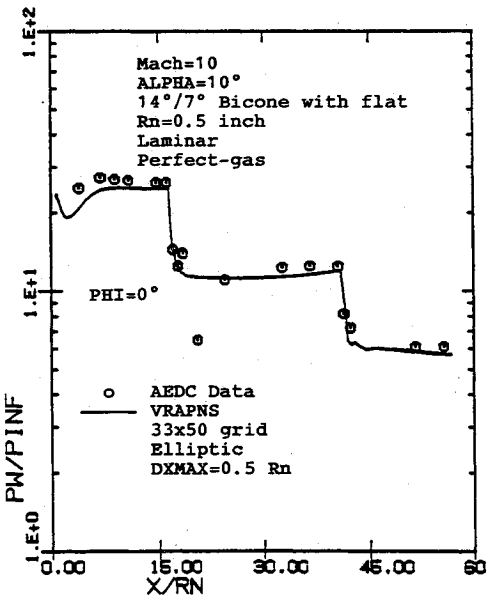


Fig. 13 Axial distribution of windward wall pressure for the bicone with flat at $\alpha = 10$ deg.

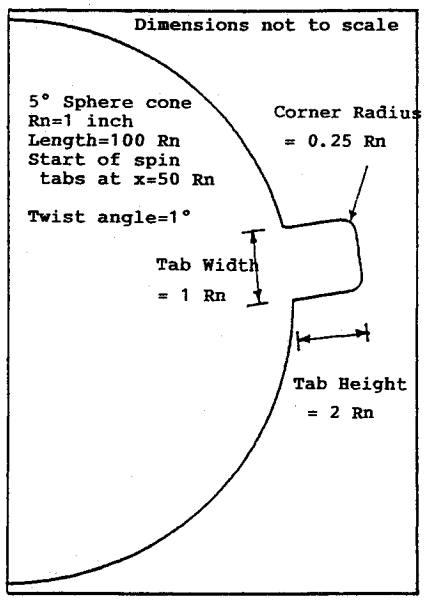


Fig. 14 Schematic description of the spin-tab geometry.

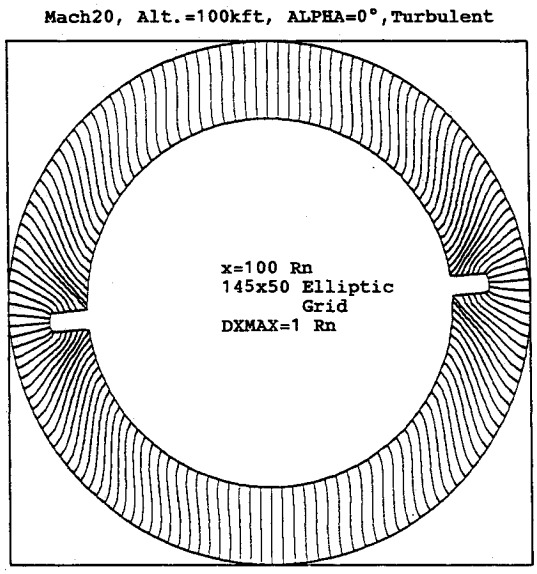


Fig. 15 The $\xi_3 = \text{const}$ coordinate lines for case 10 at $x = 100Rn$.

the computing times increase with increasing angle of attack and flow complexity. The 10-deg angle-of-attack case shows that the calculations with the elliptic grid generation took only 4% longer to do than the corresponding cylindrical grid using simple algebraic grid generation. The type of grid generation used has almost no effect on the predicted force and moment data at the body end (see Table 2). The two computational grids are compared in Fig. 10 and show that even for this relatively simple convex cross section, the elliptic grid shows a better character. The surface-orthogonal nature of the elliptic grids on the flat windward surface provides a better modeling of the near-wall viscous effects. Furthermore, the elliptic grid also provides a better modeling of the lower corner region. This is reflected in the pressure contours shown in Fig. 11, which shows that the elliptic grid provides a better and sharper description of the pressure gradients in the corner region. The results are almost identical in the remaining flow regions.

The axial distributions of wall pressure along the windward streamline for the 2- and 10-deg angle-of-attack cases are shown in Figs. 12 and 13, respectively. These predicted distributions are compared with some AEDC wind-tunnel data available for the same Mach number and freestream conditions on a bicone geometry with a similar windward flat but having an additional flat and a cut on the leeside. However, it can be appropriately assumed that under these hypersonic angle-of-attack conditions, the windward flowfield remains unaffected by the differences on the leeside. For this reason, the comparisons of Figs. 12 and 13 are indeed appropriate. These comparisons show that the present flowfield predictions are indeed in close agreement with the available data.

#### 5-Deg Sphere Cone with Asymmetric Spin Tabs

The geometry for this case (case 10) does not represent any existing configuration and was developed explicitly for demonstrating the capabilities of the elliptic grid-generation scheme and the numerical solution capabilities of the present three-dimensional PNS scheme. The geometry (Fig. 14) consists of a 5-deg sphere cone with a nose radius ($Rn$) of 1.0 in., a length of $100Rn$, and two asymmetric spin tabs that start emerging from the conical body at $x = 50Rn$ and are fully emerged by $x = 65Rn$. These spin tabs wrap around the basic body at a

constant angular rate of 1 deg (referred to as the twist angle). When fully emerged, the spin tabs are rectangular in cross section with a height-to-width ratio of 2. The tab corners are rounded, whereas their juncture with the basic body is kept sharp.

The freestream conditions used for this case are summarized in Table 1 and consist of a Mach 20 flight at 100,000 ft altitude. Only zero angle-of-attack conditions were considered, and the wall temperature was kept fixed at 2000°R. The gas model used was perfect gas, and fully turbulent flow conditions were considered. Due to the zero angle-of-attack condition used, a 1-plane axisymmetric solution was done up to $x = 45Rn$, and the full three-dimensional solution was started from this location onward.

Due to the twisting of the spin tabs around the body, the flow does not have a pitch-plane of symmetry, and the numerical solutions require a complete $0 \le \phi \le 360$ deg solution domain with periodic boundary conditions used along the $\phi = 0$ and 360-deg crossflow planes. For this case we used an elliptic grid consisting of 145 crossflow planes and 50 points between the body and the shock. The grid-generation strategy used permits the computational grid on the sides to twist around the body just as the spin tabs twist. The grid on the leeward and windward side remains fixed. Furthermore, the crossflow grid is clustered around the spin tabs such that there are a sufficient number of grid points on the top and on the sides of the spin tab. The grid at the shock is uniformly spaced to provide an accurate description of the bow shock surface. The resulting grid at the body end ($x = 100Rn$) is shown in Figs. 15 and 16. Figure 15 shows the $\xi_3 = \text{const}$ grid lines for the entire solution domain, whereas the grid detail around the spin tab is shown in Fig. 16. These figures show that the elliptic grid thus generated does indeed provide a unique combination of robustness, computational affordability, and numerical accuracy.

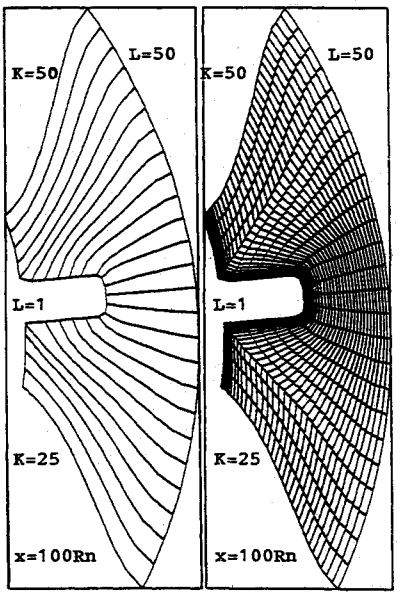


**Fig. 16 Grid details around the spin tab for the case 10 calculation at $x = 100Rn$.**

The pressure contours around the body at the body end are shown in Fig. 17 and show that the computational grid and the numerical solution do indeed capture the sharp pressure gradients around the spin tabs. When the spin tabs first emerge from the body at $x = 50Rn$, they generate a compression wave that travels down the body. As the spin tabs keep emerging, they grow in cross section until they reach the prescribed cross section (width and height) near $x = 65Rn$. From there onward, the tab cross section does not change, and thus the top surface of the tab goes through an expansion, resulting in an expansion fan that also travels down the body. Thus, when we look at the crossflow pressure contours at the body end (Fig. 17), we see that around the spin tabs there is an initial compression starting from the bow shock (which is the compression wave generated at $x = 50Rn$). This initial compression is followed by a rapid expansion (which is the expansion fan generated at $x = 65Rn$) and the subsequent compression to the top of the tab. Thus, the various flow details are accurately captured by the numerical solution. In addition, it is interesting to note that there is a complete asymmetry to the flowfield, and even the smallest details on either side are exactly replicated but not forced.

This computational solution (from $x = 50Rn$ to $x = 100Rn$) took 7 min and 6 s to do on the Cray Y/MP with a constant axial step size (DXMAX) of 1.0 $R$ and the $145 \times 50$ grid described above. These results clearly show the robustness and computational efficiency of the present elliptic grid-generation scheme over a wide range of simple to complex three-dimensional configurations. Furthermore, the stability of the numerical solution scheme is demonstrated by being able to accurately and efficiently compute the resulting complex flowfields.

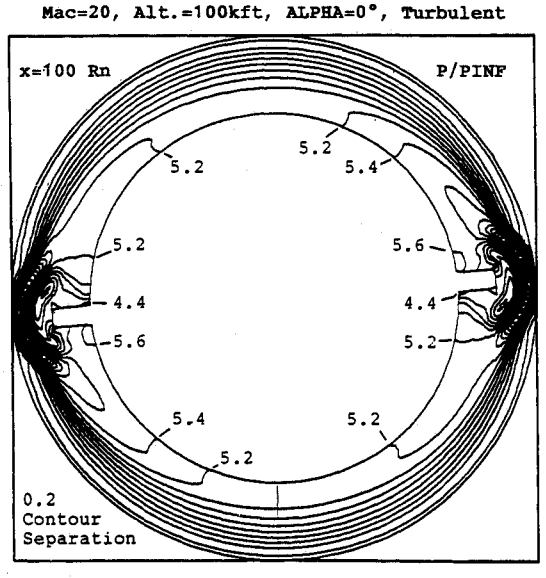


**Fig. 17 Crossflow pressure contours for case 10 at $x = 100Rn$.**

## Conclusions

Additional predictions and comparisons are provided for a new three-dimensional perfect-gas and equilibrium-air PNS scheme that has been developed to study three-dimensional hypersonic flows over complex three-dimensional configurations. These additional test cases involve three different three-dimensional configurations and cover a Mach number range of 10–20 and an angle-of-attack range of 0–14-deg. Comparisons are made with available wind-tunnel data in terms of wall-pressure distributions and force and moment data. The results of this study substantiate the following comments:

1) A new accurate and robust three-dimensional PNS scheme has been developed to study perfect-gas and equilibrium-air hypersonic flows over complex three-dimensional configurations.

2) The available grid-generation schemes include a new fast and efficient elliptic grid-generation algorithm. Although this elliptic grid generation scheme only involves 10–15% more computing time than the simplest cylindrical grid-generation schemes, it provides a very powerful and robust tool for accurately modeling complex three-dimensional configurations.

3) Force and moment data and surface pressure distributions computed for a 14/7-deg biconic configuration with/

without a windward flat surface show good agreement with the data from VKF Tunnel C at AEDC.

4) In general it is seen that for the various three-dimensional configurations tested, the numerical predictions are either in excellent agreement with available data or at worse within the uncertainty bounds of the data.

## Acknowledgments

The work reported in this paper was supported in part by the NASA Lewis Research Center under Contract NAS3-25450. The encouragement and cooperation provided by the contract monitor Tom Benson, Louis Povinelli, and Dan Whipple during the course of this effort are gratefully acknowledged.

## Reference

[1]Hahn, J. S., "Static Force Tests of Conic and Biconic Bodies at Mach Number 10," Arnold Engineering Development Center, Arnold AFB, TN, AEDC-TSR-78-V40, Nov. 1978.

Ernest V. Zoby
*Associate Editor*